

**Depth-domain processing of teleseismic receiver functions
and generalized three-dimensional imaging**

Igor B. Morozov¹ and Kenneth G. Dueker²

¹Department of Geological Sciences, University of Saskatchewan, Saskatoon, SK S7N 5E2, Canada

²Department of Geology and Geophysics, University of Wyoming, Laramie, WY 82071-3006

Submitted to *BSSA*

Revision submitted March 1, 2003

Address for correspondence:

Igor B. Morozov
Department of Geological Sciences
University of Saskatchewan
114 Science Place
Saskatoon SK S7N 5E2
Tel. 306 966 2761
Fax 306 966 8593
igor.morozov@usask.ca

Abstract

Stacking, either by itself or as a part of depth migration, is usually used for noise suppression in teleseismic receiver function (RF) images. However, stacking is neither the only signal enhancement method available, nor is it the most efficient in the environment of receiver-side source-generated noise typical for RF imaging. We generalize the pre-stack depth migration methodology by introducing numerous signal-enhancement schemes in place of final summation. The method operates in full 3-D geometry, incorporates most of the existing imaging techniques, and suggests a generalized framework of RF depth imaging. We present four applications of this technique using the data from the teleseismic Continental Dynamics-Rocky Mountains (CD-ROM) teleseismic experiment: 1) building common-image gathers to assess depth focusing of RF images, 2-3) imaging using median and coherency filters for noise suppression, and 4) generalized 3-D Common Conversion Point stacking. The results suggest that with the limited volumes and quality of the existing RF datasets, adaptive filters could be superior to record summation used in conventional depth migration.

Introduction

Teleseismic receiver functions (RF) have become an accepted standard for imaging the crust and upper mantle discontinuities (e.g., Shearer, 1991; Bostock, 1996; Dueker and Sheehan, 1998; Shen et al., 1998; Chevrot et al., 1999; Gurrola and Minster, 2000). RF techniques are viewed as the primary source of detailed information on the *S*-wave velocity contrasts within the upper mantle. However, the existing RF depth imaging still lags behind its counterpart in reflection seismology, firstly, in the use of 2-D approximations instead of full 3-D imaging, and secondly, in the lack of processing approaches that could be used to validate the image by observations of “events” in the records. For example, although pre-stack RF depth migration is based on the underlying forward *P*- to *S*-wave scattering model that is undoubtedly correct, it still does not include tools that could help determine what part of the recorded wavefield actually complies with this wave propagation model. Also, it is usually assumed that record summation is adequate for extraction of the desired modes from the recorded wavefield, but verification of this sufficiency presents serious difficulties with real RF data.

The existing RF imaging is based on techniques borrowed from exploration reflection seismics and includes moveout corrections, common conversion point (CCP) stacking (Dueker and Sheehan, 1998; Zhu, 2000), velocity spectrum stacking (Gurrola et al., 1994; Shen et al., 1998), τ -*p* record interpolation (Neal and Pavlis, 1999), and several types of pre-stack depth migration (e.g., Sheehan et al., 2000; Bostock et al., 2001, Bostock, 2002). However, RF recordings, with limited-apertures receiver arrays or single stations, relatively sparse and uneven source distributions, lower data redundancy and signal-to-noise ratios, are vastly different from exploration reflection records. Consequently, reflection imaging methods require cautious and critical modifications when applied to RF data.

Below, we propose a general paradigm of 3-D RF depth imaging, attained by relaxing two assumptions implicit to pre-stack depth migration. First, instead of simply assuming that the recorded wavefield agrees with a chosen mode conversion model, we aim to provide tools that could help test this assumption. Second, we no longer assume that stacking is sufficient for attenuation of the coherent noise and allow inclusion of numerous data-dependent signal detection schemes that may be introduced by the interpreter.

With specific choices of time-to-depth mapping schemes and treatment of amplitudes, this generalized approach incorporates most of the existing methods of pre-stack RF depth migration or CCP stacking. Regardless of its specific type, imaging is always performed in 3-D. The imaging procedure is explicitly subdivided into three steps, each of which is implemented and tested independently: 1) time-domain processing, 2) time-to-depth mapping, and 3) depth-domain processing. We emphasize the extensive depth-domain analysis as the key component required for isolation of the mode of interest as opposed to coherent and incoherent noise. Such detailed, pre-stack analysis is also quite practical computationally due to small volumes of RF datasets.

Multiple depth-domain processing (hereafter DDP) choices lead to multiple images, and this multiplicity may seem to complicate the interpretation. However, RF depth imaging is already an inherently strongly underconstrained and inconsistent inverse problem, and the properties of the inversion procedures (e.g., data editing, filtering, algorithm types, and regularization) leave strong impacts on the results. For example, the results of pre-stack depth migration are influenced by the chosen *a priori* forward model (including assumptions of the mode content of the wavefield and relative weighting of the modes), by the choice of the Born vs. Kirchhoff approximation (Bostock, 2002), dip filtering (Lafond and Levander, 1993), transformation of surface and emergence angle integrations into summations (Bostock et al., 2001), other types of “pre- and post-conditioning”

(Chavent and Plessix, 1999), or by a choice of a single-pass migration or iterative inversion. Underlying processing causes uncertainty of RF images that is expressed in variations of the structural types of images produced and in potential artifacts. This uncertainty may be greater than usually acknowledged and is a source of concern. and. In the “multi-processing” approach facilitated by the DDP method, we provide means for assessment (however, still not the final judgment!) of the viability of the various imaging strategies.

A serious vulnerability of the conventional RF processing, particularly at frequencies above ~ 0.5 Hz, is the potential for imaging artifacts caused by crustal scattering (e.g., Bannister et al., 1990; Gupta et al., 1990; Wagner and Langston, 1992; Clouser and Langston, 1995; Abers, 1998; Revenaugh, 2000; Bertrand et al., 2002). The background of receiver-side signal-generated noise may be indistinguishable from mode conversions in the final (even stacked or migrated) image. Imaging artifacts from stacking direct and guided waves are well known in reflection seismics, and practically the only recognized way to suppress such artifacts is to identify, isolate, and attenuate them in the pre-stack domain (e.g., Steeples and Miller, 1998). Extension of such pre-stack analysis to RF imaging is the primary objective of the DDP method.

Below, after an overview of the concept of the Common Image Gathers that is central to DDP, we describe our generalized 3-D RF imaging method. In the following examples, we present CIGs of real RF data from the CD-ROM experiment (Dueker et al., 2001; Morozov and Dueker, 2003), and give three alternative CD-ROM depth images. Finally, we discuss the interpretation of these images and also show that the Common Conversion Point stacking represents a special case of the new approach, with all the advantages of the generalized DDP.

Common-Image Gathers in RF imaging

For a given surface point (\mathbf{I}_s in Fig. 1), a Common Image Gathers (CIG) is obtained simply by mapping all (or a subset of) the input time-domain RF records into depth under that point (CIG “well” in Fig. 1). Summation of such depth-mapped records within a CIG results in the pre-stack depth-migrated image under that point. However, prior to (or instead of) such summation, additional useful information could be obtained from the CIG, and numerous imaging techniques could be devised through CIG processing.

In exploration and crustal reflection seismics, CIGs are used for velocity analysis in pre-stack depth migration (Al-Yahya, 1989; Lafond and Levander, 1993). Theoretically, when displayed sorted by the source-receiver offsets, the records in a CIG show depth-offset moveouts related to errors in the background migration velocity model. In RF imaging, the ray parameter is as an equivalent to the offset, and therefore event moveouts (variations of their time with p) in a CIG can be directly related to the errors in background velocities (Al-Yahya, 1989). However, in the RF case, the sensitivity of these moveouts to velocity errors is weak. For example, it can be shown that for a $PpDs$ conversion from the Moho, a 10% increase of bulk V_S of the crust (keeping V_P fixed) would result in a CIG moveout below 0.5% within the typical RF ray-parameter range. Therefore, with reasonable velocity uncertainties, all the $PpDs$ events in a CIG should be always nearly horizontal, and prevalence of strongly dipping events would indicate seismic phases that are not accounted for by the chosen mode kinematics (reverberations and shallow, broadside scattering).

Using the DDP scheme permits the analysis and processing of each of the CIGs individually before they are assembled into a final image. In cases when scattered events can be identified in CIG gathers, one could also design a filter to suppress these noise events. Processing

thus becomes data- and target-dependent, and consequently no universal imaging recipe can be prescribed for all cases. Instead, in each particular case, one should interpret the causes of CIG event misalignments and build a DDP filter attenuating these mis-aligned events.

Generalized 3-D pre-stack depth migration

By including a depth signal detection step into pre-stack depth migration (Morozov and Levander, 2002) the latter method is extended into a broad class of RF imaging schemes. Owing to its kinematic equivalence to Born or Kirchhoff pre-stack depth migration (e.g., Sheehan et al., 2000; Bostock et al., 2001, Bostock, 2002), all the arguments in favor or against such migration hold for this approach as well. However, an important difference of DDP migration from the existing RF migration schemes is its full 3-D formulation.

Recognizing the fact that seismic velocities (and hence timing of teleseismic arrivals) are relatively accurately known but the amplitudes of RFs are often contaminated with strong noise (leading to image coherency $\ll 1$, cf. Morozov and Dueker, 2003), we compensate the predictable kinematics of the seismic phase of interest (in this case, the $P_D S$ or $Pp_D S$ mode conversion) and focus on the resulting event alignment (phasing). A compact formulation of this approach arises from pre-stack depth migration as an inverse of the following forward problem, in matrix form (e.g., Chavent and Plessix, 1999):

$$\mathbf{WU} = \mathbf{WBR} . \quad (3)$$

Here, \mathbf{U} is the recorded RFs, \mathbf{R} is the conversion amplitude of interest, \mathbf{B} is the propagator (e.g., a combination of the source and receiver Green's functions), and \mathbf{W} is a diagonal weight ("preconditioning") matrix. For a given recording time t , matrix product (3) is reduced to summation over the surface $t=const$ ("scattering ellipsoid") within the model. An important application of \mathbf{W} is "dip equalization" transforming the summations over the recording surface

into a summation over ray directions at the imaging point (often referred to as the generalized Radon transform, cf. Beylkin and Burrige, 1990; for recent applications to RF, see Bostock et al., 2001, and Bostock, 2002).

Direct, and even iterative inversion of system (3) is often computationally prohibitive, and, because of high noise levels, it could also be meaningless in RF imaging. An inexpensive, one-pass, approximate inverse (usually called “migration”), is obtained by using the “back-projection” operator \mathbf{B}^T (T denotes the matrix transpose) multiplied by some diagonal, “post-conditioning” matrix \mathbf{K} (Chavent and Plessix, 1999):

$$\mathbf{R} = \mathbf{K}\mathbf{B}^T \mathbf{W}^T \mathbf{W}\mathbf{U} \equiv \sum_i \mathbf{F}\mathbf{U}_i, \quad (4)$$

where $\mathbf{F} = \mathbf{K}\mathbf{B}^T\mathbf{W}$. Expression (4) renders the depth image (\mathbf{R}) as a sum of RFs (\mathbf{U}_i), converted to depth, weighted to compensate the geometric spreading, and preconditioned. The operator \mathbf{F} represents the resulting mapping of the RF time series into depth at every imaging point (Fig. 1). Depending on the choice of \mathbf{B} , \mathbf{W} and \mathbf{K} , this mapping may include amplitude corrections to compensate the geometric spreading, uneven source-receiver distribution, and also the uneven azimuthal, dip, and ray parameter coverage of the subsurface.

The purpose of matrix \mathbf{K} in equation (4) is to provide the appropriate scaling of the resulting model; one example is $\mathbf{K}=\text{diag}(\mathbf{B}^T\mathbf{W}^T\mathbf{W}\mathbf{B})^{-1}$ corresponding to the “true-amplitude” approximation (Chavent and Plessix, 1999). As with any underconstrained problem, there exist various choices for \mathbf{K} (e.g., “mass lumping”, Chavent and Plessix, 1999). The data weights \mathbf{W} may include “obliquity” and “dip equalization” factors; combined with the forward model \mathbf{B} and regularization parameters, these factors control the trade-off between model resolution and variance. Combined choices of operators \mathbf{B} , \mathbf{K} , and \mathbf{W} yield multiple possible migration schemes,

of which perhaps the most notable are a group of Generalized Radon Transform methods (Bostock et al., 2001; Bostock 2002).

With a large variety of possible migration approaches, it is important to realize, however, that elaborate inversion schemes, relying on subtle amplitude correlations among the records, is hardly warranted by the strong level of noise and sparse sampling of the 5-dimensional data space. For this reason, below, we concentrate on a more modest task assessing the consistency of RF phasing. For this purpose, it is sufficient to choose unit matrices for \mathbf{W} and \mathbf{K} , and use a simple asymptotic approximation for \mathbf{B} based on geometric ray spreading (Vidale and Houston, 1990).

For a single imaging point, migration result (Eqn. 4) is a sum of the input RF waveforms, transformed to depth and taken with the appropriate weights. At this point, we no longer rely on the cancellation of noise amplitudes through summation (Eqn. 4), but replace it with a general combination of depth-mapped records:

$$\mathbf{R} = \Psi(\mathbf{FU}_1, \mathbf{FU}_2, \mathbf{FU}_3, \dots). \quad (5)$$

This (in general) non-linear operator Ψ can now include scaling, filtering, signal enhancement (such as various kinds of stacking, median, principal-component or coherency filtering), record normalization, sorting, display, and other operations. The resulting imaging method (5), therefore, can be better described in algorithmic fashion, as a depth-domain seismic processing (DDP) sequence:

For every surface location (X, Y) and for each RF record \mathbf{U}_i :

DDP.1) Map all the input RFs to depth at this location, using 3-D ray kinematics (\mathbf{FU}_i).

DDP.2) Form a section of depth-domain records \mathbf{FU}_i .

DDP.3) Process the section obtaining one or several output records $\Psi(\dots)$.

DDP.4) Sum the resulting records $\Psi(\dots)$ and place them at the location (X, Y) within the model.

Step DDP.1 above is purely model-based (Fig. 1) and is carried out (provided that the background velocity structure is known) with a high degree of certainty and independently of the data quality. By contrast, the amplitude and phasing analysis DDP.3 is performed within a flexible processing sequence and should combine various tools in order to isolate scattering artifacts and other adverse factors. Without this step, the approach is equivalent to the traditional Kirchhoff pre-stack depth migration.

Although DDP procedure is simple and straightforward, it requires a specialized seismic processing package that allows user-defined seismic processing flows embedded within the migration loop. We utilized an object-oriented seismic processing approach by Morozov and Smithson (1997) that has been recently expanded with tools for travel-time-map-based migration (Morozov and Levander, 2002) and for handling teleseismic records. An advantage of the modular design is in utilization of a number of migration weighting schemes and a dip filter controlled by the choice of parameters \mathbf{B} and \mathbf{W} in operators (Eqn. 4). Similarly to commercial seismic processing systems, the entire DDP procedure is described using a specialized scripting language providing access to over a hundred processing tools without the need for computer programming (Morozov and Smithson, 1997). Below, we present four applications of this technique.

Real-data examples of depth-domain RF processing

We start with three types of multichannel RF processing that provide insight into the construction of a pre-stack RF image. We use teleseismic data from a broadband teleseismic array deployed as a part of the Continental Dynamics of the Rocky Mountains (CD-ROM) experiment recorded from June 1999 to June 2000 (Dueker et al., 2001). Of the two CD-ROM deployments, we choose the northern part consisting of 21 stations spaced at about 10-12 km (Fig. 2). This array is one of several relatively large and dense PASSCAL arrays operated recently and provides a good datasets

for detailed analysis of the crust and upper mantle. Targeting the variations of lithospheric properties across the Cheyenne suture, we placed the 3-D imaging grid with horizontal and vertical spacing of 2.5 km centered under the array (Fig. 2). Although the array is nearly linear, and therefore provides usable resolution only along its axis, we performed 3-D imaging to account for out of plane back-azimuths (Fig. 1). For time-to-depth mapping, we utilized the IASPEI91 model; as the sensitivity of RFs to velocity variations is relatively low, this model is sufficient for our illustration of DDP techniques.

Common-Image Gatherers of real CD-ROM RF data

To create a CIGs for a selected point of the imaging grid (Fig. 2), we performed DDP migration into that point with the DDP.3 flow consisting of a trace display sorted by the absolute value of ray parameter (p). In the resulting pre-stack CIG section (Fig. 3), the Moho can be traced relatively unequivocally at ~40-km depth. However, below the Moho, the resulting image shows poorer coherency. Since errors in the background velocity model can account for small CIG moveouts, any misalignment of the records should be due to crustal scattering, site effects, and contributions from converted modes different than $P_D S$. However, with relatively few records in the CIG, it is difficult to isolate noise wavetrains without extensive dip filtering in the depth-ray parameter domain. Such filtering can be applied (see Example 3), yet it also involves a danger of over-processing.

Two conclusions can be drawn from an inspection of real-RF-data CIGs: 1) significantly larger data volumes are required for reliable imaging below the Moho (at least, for this data set), and 2) since CIG coherency is not apparent and the numbers of records in the existing datasets are limited, robust signal detection schemes (not simply relying on record summation) are needed in order to improve imaging. In the following examples, we experiment with two possible schemes of this kind.

Generalized pre-stack depth migration

Median filtering is broadly accepted as a statistically stable signal estimator in the background of strong noise. Its stability is due to relative insensitivity of the median to large-amplitude outliers; by contrast, with low-fold stacking, such outliers can dominate the average.

To incorporate median filtering into depth migration, the records were sorted by the ray parameter and included a sample-by-sample median filter into step DDP.3 of our procedure. Although it is possible to apply a median filter to all of the records within a CIG, we chose to apply this filter within a running trace window. For each of the CIGs corresponding to the individual imaging locations (Fig. 3), a window of 20 records was arranged, moving from one end of the CIG to another. For each window position, a sample-by-sample median of the records was computed and assigned to the trace at the middle of the window (Fig. 3b).

As explained above, in depth-domain imaging, we are only interested in the events with zero moveouts. Nevertheless, strong signal generate noise and reverbs with non-zero moveouts are present in the CIGs, if not dominate them (Fig. 3). Coherent noise is particularly dangerous because it will stack constructively and produce spurious events in the final image. Therefore, a more robust strategy for event enhancement could consist in detection of the strongest noise (non-horizontal in the depth domain) events, and in their removal from the CIGs. To detect such events, we experimented with a coherency filter similar to that routinely applied to CDP crustal datasets of the Canadian Lithoprobe program (Milkereit and Spencer, 1989).

In this method, we arranged the same sliding windows within the CIGs as above, and within each of these windows computed 21 slant stacks within the range of moveouts from -2000 to 2000 $\text{km}/(\text{s}\cdot\text{km}^{-1})$. For each of these moveouts, the “semblance” was defined as the ratio of the stack power along this moveout to the maximum stack power among all of the moveouts examined. Further, local

(depth-and *ray parameter* dependent) “coherency” was defined as semblance raised to a power of $\gamma=2$ (the typical choices for γ are between 1 and 2; Milkereit and Spencer, 1989). This coherency was used as stacking weight emphasizing the strongest linear events. Finally, such events with nonzero moveouts were removed from the output of our filter. The resulting filtered CIGs (Fig. 3c) show marked differences from the unprocessed gather (Fig. 3a). The Moho stands out better throughout the entire range of ray parameters, and discontinuities below 80-km depths is more apparent (Fig. 3c).

By applying the three depth-domain filters at each surface location (Fig. 1), we obtained the corresponding migrated images (Fig. 4). We deliberately extended our imaging grid by ~ 40 km beyond the ends of the array (line X-X' in Fig. 2), so that migration artifacts at the ends of the array are apparent and may be compared with similar features within the section (Figs. 4). Somewhat surprisingly, the running (20-trace) median filtering resulted in a less coherent image compared to the straight stack (Figs. 4b and a, respectively). Non-linear slant filtering resulted in the most coherent cross-section (Figs. 4c).

The resulting images have many common features, and we consider these consistent features to be robust (Fig. 5): a gap in the Moho, a step in crustal thickness across the Cheyenne Belt, and north-dipping contrasts within the mantle at 90-120 km depth beneath the CB. However, at greater levels of detail the migrated images in Fig. 4 show significant differences. A possible approach to interpretation could thus be to identify the features that are consistent across the variety of processing choices, particularly among those using the more stringent signal detectors (e.g., pre-stack coherency filtering).

Common conversion point stacking

Common-Conversion Point (CCP) stacking is an established method of array RF imaging (e.g., Dueker and Sheehan, 1998; Zhu, 2000; Dueker et al., 2001). Based on an approximation of horizontally layered Earth and uniform $P_D S$ conversion amplitudes, diffractions are ignored in CCP

mapping, resulting in increased continuity of the image within the crust and higher horizontal detail deeper within the mantle. CCP stacking could thus be preferable when there is sufficient evidence for predominantly horizontal layering.

CCP stacking can also be rendered in the form of our DDP process with the time-to-depth mapping performed differently (Fig. 6b). Provided the background velocity is known, CCP time-to-depth mapping is controlled by the horizontal “bin-sharing” distance, b (Fig. 6b; Dueker and Sheehan, 1998; Zhu, 2001). For an imaging point, \mathbf{I} , only RFs with their corresponding conversion (“piercing”) points, \mathbf{C} , within distance b from \mathbf{I} are considered (Fig. 6b). RF amplitudes mapped into depth at points \mathbf{C} are summed yielding the CCP stack at \mathbf{I} .

Fig. 4d shows an axial slice through 3-D CCP stack computed using bin-sharing distance of 20 km (Dueker et al., 2001). Along with similar features to the migrated images (Fig. 4a-c), the two strong distinctions of the CCP stack are the spurious event at zero depth (caused by stacking of the zero-lag RF pulse corresponding to the direct P -wave) and a smoother and stronger Moho, with a significantly narrower gap in the region of Cheyenne belt (Figs. 4). Both of these features, however, are artifacts of CCP stacking caused by a fixed horizontal bin sharing exceeding the Fresnel zone at the Moho depth. By contrast, migration (Fig. 4) appears to be more successful in focusing the dipping events from 90-120-km depth.

Discussion and conclusions

Because of the proximity of coherent noise to useful signal, multichannel depth RF imaging differs from exploration seismology and is probably closer to shallow reflection seismics. In such environment, special processing and interpretational approaches are required in order to avoid misinterpretation (Steeple and Miller, 1998). The DDP scheme could alleviate this problem by offering a general, yet standardized, control of the numerous aspects of image formation by: (1)

providing a uniform three-step formulation encompassing many of the existing RF depth imaging techniques; (2) encouraging pre-stack visualization and filtering of the records in the depth domain in which the validity of the forward model can be effectively tested; and, (3) offering “multi-processing” in order to facilitate assessment of the impact of processing and inversion on the final image.

The two most important features of the DDP framework are its inherent 3-D character and explicit separation of the time-to-depth mapping from the subsequent processing in depth domain. For given target mode, DDP is focused on a single depth point, with all the true events aligned horizontally. Such alignment simplifies coherency analysis, and a variety of filtering and processing tools could be included in this environment. The aim of such processing would be to detect and/or enhance horizontally aligned energy in a multichannel record – a relatively simple task given the vast experience in signal processing accumulated in reflection seismology. A few potentially useful approaches in addition to those illustrated above include: diversity stack (Embree, 1968), optimal filters (e.g., Rietsch, 1980), principal-component (Karhunen-Loève, SVD) filters (Hemon and Mace, 1978), sign statistic filters (Hansen et al., 1988), f - x deconvolution, correlation autostatics, and other coherency filters. DDP can also incorporate bootstrapping of the data volume (Sheehan et al., 2000; Morozov and Dueker, 2003) to assess the image errors and artifact.

Given that the image is conditioned by the algorithm, comparison of several imaging schemes (Figs. 4a-d) applied to the same data (and using the same 3-D imaging grid and velocity model) would provide a basis for checking their respective underlying assumptions. For example, the CCP stack shows an apparently greater continuity and amplitude of the Moho and suggests several south-dipping events below about 80 km within the mantle (Fig. 4d). However, in the

migrated images, this depth range is dominated by north-dipping events, at least in the northern part of the array (Fig. 4a-c). Since neither of our migration schemes includes any enhancement of lateral coherency, appearance of these continuous events supports their authenticity.

Failure of the median-filtered migration to produce an improved image compared to the straight stack (Fig. 4b) is somewhat disconcerting. Median filtering is generally considered to be a robust approach to averaging noisy data; however, in our case, the unfiltered and coherency-filtered migrations perform better. This observation may reflect the difference between the visual appeal of the image (e.g., judged by the continuity of the boundaries) and its internal consistency, and therefore the median-filtered image may indeed indicate insufficient sampling. This problem should be alleviated with acquisition of larger data volumes.

By relaxing the emphasis on elaborate forward models and inverse solutions, the DDP method offers a simple and uniform approach to 3-D imaging. Given the heterogeneity of the crust and mantle, and the noise levels in RF records, mapping of mantle structures should be naturally performed in 3-D (Fig. 4). Note that despite the similarity in the in-line migrated images (Fig. 4) differences, the horizontal slices are strikingly different (Fig. 7), suggesting a 3-D structure and also sampling decrease towards the edges of the 3-D volume. However, a larger, true 3-D dataset is required for further assessment of the properties of 3-D imaging. When carefully implemented, generalized 3-D DDP migration is also quite affordable. In our examples (Figs. 2, 4), migration of the entire dataset (~2000 RFs) took only about 15-40 min on a 2-GHz Linux PC, depending on the types of embedded filtering utilized.

Finally, the potential of DDP extends far beyond the examples presented above. Virtually any of the existing RF depth imaging schemes can be incorporated via this approach, with the advantages of 3-D imaging and robust signal detection. Other types of travel-time mapping (e.g.,

targeting surface waves or using heterogeneous, 3-D travel-time models) and plane-wave migration (Poppeliers and Pavlis, in review) could be incorporated. Array-based methodologies for computing RFs (Li and Nábělek, 1999) could also benefit from their implementation in the depth domain. This method should also provide the means for quality control (Morozov and Dueker, 2003) and statistically robust ways to perform imaging using other signal-detection techniques yet to be explored.

Acknowledgements

We are grateful to IRIS PASSCAL program that made the data acquisition possible. Comments by two anonymous reviewers and the Associate Editor Lorraine W. Wolf have helped in improving the manuscript. This research was supported by NSF Grant EAR99-03235. I. M. was also supported in part by the Defense Threat Reduction Agency Grants DTRA01-01-C-0057 and DTRA01-01-C-0081.

References

- Abers, G. A. (1998). Array measurements of phase used in receiver function calculations: Importance of scattering, *Bull. Seism. Soc. Am.*, **88**, 313-318.
- Al-Yahya, K. (1989). Velocity analysis by iterative profile migration, *Geophysics*, **54**, 718-729.
- Bannister, S. G., E. S. Husebye, and B. O. Ruud (1990). Teleseismic *P* coda analyzed by three-component and array techniques: deterministic location of topographic *P*-to-*R_g* scattering near the NORESS array, *Bull. Seism. Soc. Am.*, **80**, 1969-1986.
- Beylkin, G., and R. Burridge (1990). Linearized inverse scattering problems in acoustics and elasticity, *Wave Motion*, **12**, 15-52.

- Bertrand, E., A. Deschamps, and J. Virieux, Crustal structure deduced from receiver functions via single-scattering migration, *Geophys. J. Int.*, 150, 524-541, 2002.
- Bostock, M. G. (1996). Ps conversions from the upper mantle transition zone beneath the Canadian landmass, *J. Geophys. Res.*, **101**, 8383-8402.
- Bostock, M. G. (2002). Kirchhoff-approximate inversion of teleseismic wavefields, *Geophys. J. Int.*, **149**, 787-785.
- Bostock, M. G., S. Rondenay, and L. Shragge (2001). Multi-parameter 2-D inversion of scattered teleseismic body waves – I. Theory for oblique incidence, *J. Geophys. Res.*, **106**, 30,771-30,782.
- Chavent, G., and R.-E. Plessix (1999). An optimal true-amplitude least-squares depth-migration operator, *Geophysics*, **64**, 508-515.
- Chevrot, S., L. Vinnik, and J. P. Mintagner (1999). Global-scale analysis of the mantle Ps phases, *J. Geophys. Res.*, **104**, 20,203-20,219.
- Clouser, R. H., and G. A. Langston (1995). Modeling observed P-Rg conversions from isolated topographic feature near the NORESS array, *Bull. Seism. Soc. Am.*, **85**, 195-211.
- Dueker, K. H. Yuan, and B. Zurek (2001). Thick Structured Proterozoic Lithosphere of the Rocky Mountain Region, *GSA Today*, **4**, 3-9.
- Dueker, K. G., and A. F. Sheehan (1998). Mantle discontinuity structure beneath the Colorado Rocky Mountains and High Plains, *J. Geophys. Res.*, **103**, 7153-7169.
- Embree, P., Diversity seismic record stacking method and system, U.S. Patent No. 3,398,396.

- Fuchs, K., and G. Müller (1971). Computation of synthetic seismograms with the reflectivity method and comparison with observations, *J. R. Astronom. Soc.*, **23**, 417-433.
- Gupta, I. N., C. S. Lynnes, T. W. McElfresh, and R. A. Wagner (1990). F-K analysis of NORESS array and single-station data to identify sources of near-receiver and near source scattering, *Bull. Seism. Soc. Am.*, **80**, 2227-2241.
- Gurrola, H., and J. B. Minster (2000). Evidence for local variations in the depth to the 410-km discontinuity beneath Albuquerque, New Mexico, *J. Geophys. Res.*, **105**, 10,847-10,856.
- Gurrola, H., J. B. Minster, and T. Owens (1994). The use of velocity spectrum for stacking receiver functions and imaging upper mantle discontinuities, *Geophys. J. Int.*, **117**, 427-440.
- Hansen, K. M., R.-C. Chowbury, and R. A. Phinney (1988). The sign filter for seismic event detection, *Geophysics*, **55**, 1024-1033.
- Hemon, C. H., and D. Mace (1978). Use of Karhunen-Loeve transformation in seismic data processing, *Geophys. Prosp.*, **26**, 600-606.
- Karlstrom, K. E., and R. S. Houston (1984). The Cheyenne Belt: Analysis of a Proterozoic suture in southern Wyoming, *Precambrian Research*, **25**, 561-576.
- Lafond, C. F. and A. Levander (1993). Migration moveout analysis and depth focusing, *Geophysics*, **58**, 91-100, 1993.
- Li, X. and J. L. Nábělek (1999). Deconvolution of teleseismic body waves for enhancing structure beneath a seismometer array, *Bull. Seism. Soc. Am.*, **89**, 190-201.

Milkereit, B., and C. Spencer (1989). Noise suppression and coherency enhancement of seismic data; in Bonham-Carter, F. P. (Ed.) Statistical application in the Earth sciences, Geological Survey of Canada, Paper 89-9, 243-248.

Morozov, I. B., Slab or trench? On the importance of crustal scattering in receiver function imaging, *J. Geophys. Res.*, in review (see <http://w3.uwyo.edu/~morozov/st.pdf>)

Morozov, I. B. and A. Levander, Depth image focusing in travel-time map based wide-angle migration, *Geophysics*, 67 (6), 1903-1912, 2002.

Morozov, I. B. and K. G. Dueker (2003). Signal-to-noise ratios of teleseismic receiver functions and effectiveness of stacking for their enhancement, *J. Geophys. Res.* Vol. 108, No. B2, 10.1029/2001JB001692, 2003.

Morozov, I. B., and S. B. Smithson (1997). A new system for multicomponent seismic processing, *Computers & Geosciences*, **23**, 689-696.

Nabelek, J., X.-Q. Li, S. Azevedo, J. Braunmiller, A. Fabritius, B. Leimer, A. M. Tréhu, and G. Zandt (1993). A high-resolution image of the Cascadia subduction zone from teleseismic converted phases recorded by a broad-band seismic array, *Eos, Trans. AGU*, 74(43), Fall. Meet. Supl., 431,

Neal, S. L., and G. L. Pavlis (1999). Imaging *P*-to-*S* conversions with multichannel receiver functions, *Geophys. Res. Lett.*, **26**, 2581-2584.

Poppeliers, C. and G. L. Pavlis, in review. Three-dimensional, prestack, planewave migration of teleseismic *P*-to-*S* converted phases I: Theory, *J. Geophys. Res.*.

- Revenaugh, J. (2000). The relation of crustal scattering to seismicity in Southern California, *J. Geophys. Res.*, **105**, 25,403-25,422.
- Rietsch, E. (1980). Estimation of the signal-to-noise ratio of seismic data with an application to stacking, *Geophys. Prosp.*, **28**, 531-550.
- Shearer, P. M. (1991). Constraints on upper mantle discontinuities from observations of long-period reflected and converted phases, *J. Geophys. Res.*, **96**, 18,147-18,182.
- Sheehan, A. F., Shearer, P., Gilbert, H. J., and Dueker, K. G. (2000). Seismic migration processing of P-SV converted phases for mantle discontinuity structure beneath the Snake River Plain, western United States, *J. Geophys. Res.*, **105**, 19,055-19,065.
- Shen, Y., S. C. Solomon, I. T. Byarnason, and C. J. Wolfe (1998). Seismic evidence for a lower-mantle origin of the Iceland Plume, *Nature*, **395**, 62-65.
- Steeple, D. W., and R. D. Miller (1998). Avoiding pitfalls in shallow seismic reflection surveys, *Geophysics*, **63**, 1213-1224.
- Vidale, J. E., and H. Houston (1990). Rapid calculation of seismic amplitudes, *Geophysics*, **55**, 1504-1507.
- Wagner, R. A., and G. A. Langston (1992). Body-to-surface wave scattered energy in teleseismic coda observed at the NORESS seismic array, *Bull. Seism. Soc. Am.*, **82**, 2126-2138.
- Zhu, L. (2000). Crustal structure across the San Andreas Fault, Southern California from teleseismic converted waves. *Earth Planet. Sci. Lett.* **179**, 183-190.

FIGURES (for larger figures, see pages following the corresponding captions)

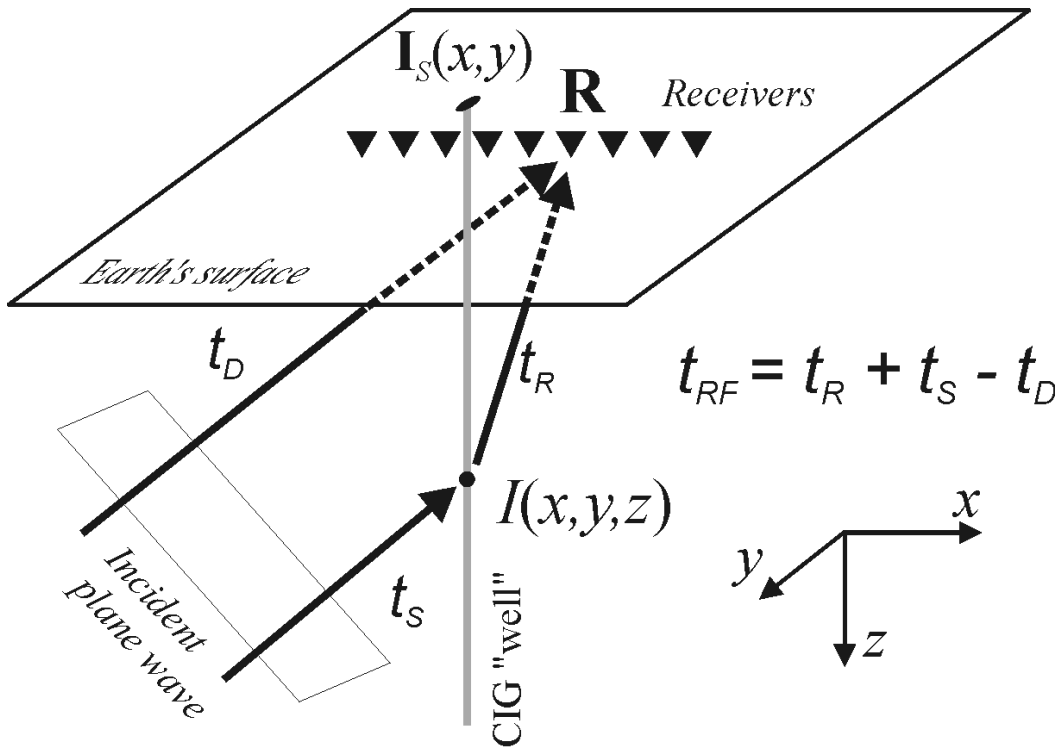


Fig. 1. Time-to-depth mapping of a $P_D S$ mode used in pre-stack depth migration and in the formation of the Common-Image Gathers (CIGs). For each of the incident P waves, travel times (t_S) of the surface reflection to every point within the model are precomputed and stored. For each of the receivers, \mathbf{R} , the S -wave travel times to every point of the model are also precomputed. Further, for each RF record and imaging point $I(x, y, z)$, the corresponding travel-time maps are combined to form the predicted RF time, $t_{RF}(x, y, z)$ ($t_D = t_S(\mathbf{R})$ is the time of the primary arrival): For any surface location (x, y) , the inverse of this function yields the desired mapping: $t_{RF} \rightarrow z$. The travel times are modeled in a 3-D (V_P, V_S) velocity distribution (however, we used a 1-D IASP91 model in this study) using an eikonal travel-time solver.

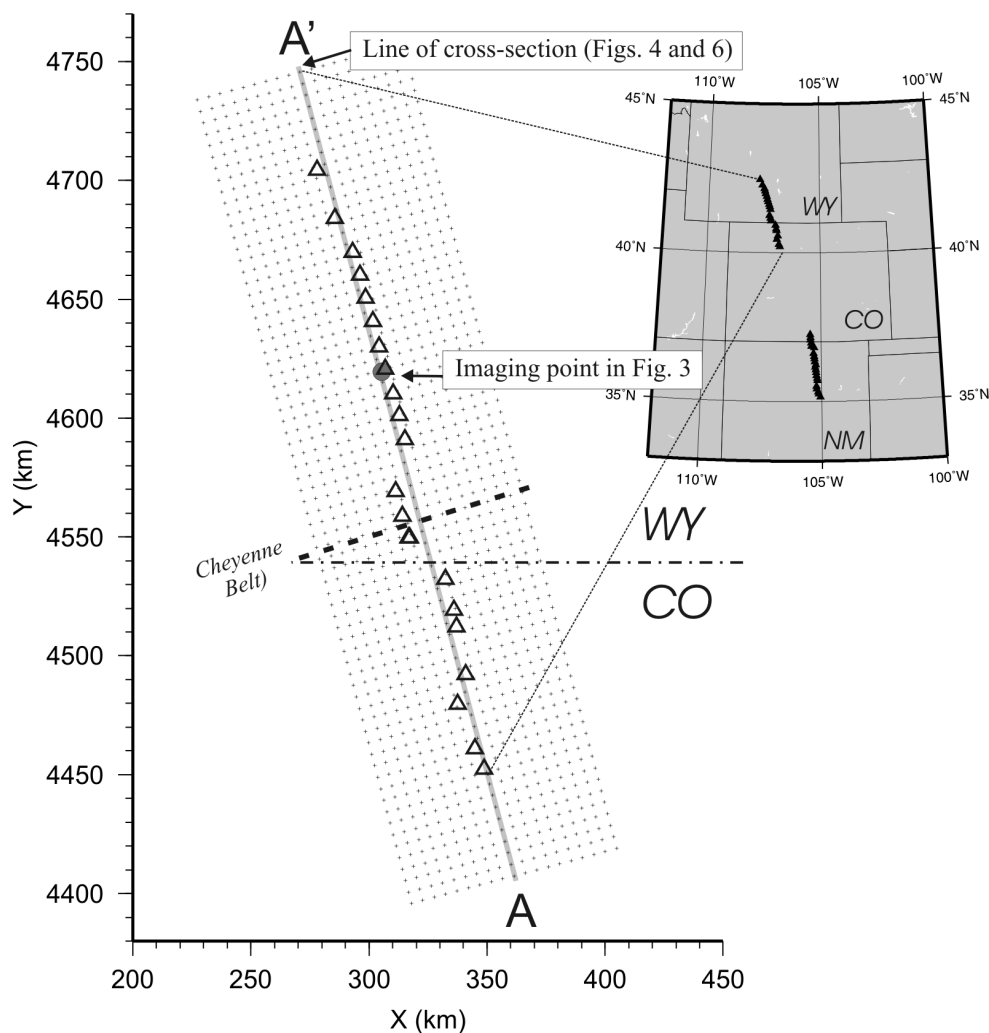


Fig. 2. The northern part of the CD-ROM array. The approximate location of the Cheyenne Belt is shown with a thick dashed line. The rectangular imaging grid is also shown, decimated to every 4-th node for clarity. The node at km 50 along the axis of the array and the line of a cross-section used in the examples are highlighted in gray. Coordinates are the Universal Transverse Mercator (UTM); inset shows the location of the entire CD-ROM array. Stations are triangles. WY and CO are the states of Wyoming and Colorado respectively.

Fig. 3. Common image gather (CIG) for the center of the imaging grid (large gray dot in Fig. 2):

(a): after conventional processing; a stack of these records constitutes the traditional pre-stack depth migrated image at the center of the array (Fig. 4, top). (b) The same CIG after median filtering within a sliding window of 20 records. (c) The same CIG processed using a slant filter enhancing all events within a range of depth moveouts between ± 2000 $\text{km}/(\text{s}\cdot\text{km}^{-1})$. Note the strong non-horizontal noise events marked with gray arrows. (d) The same CIG after application of a non-linear slant filter designed to reject the non-horizontal depth moveouts. These CIGs are used to build the corresponding depth-migrated images in Fig. 4.

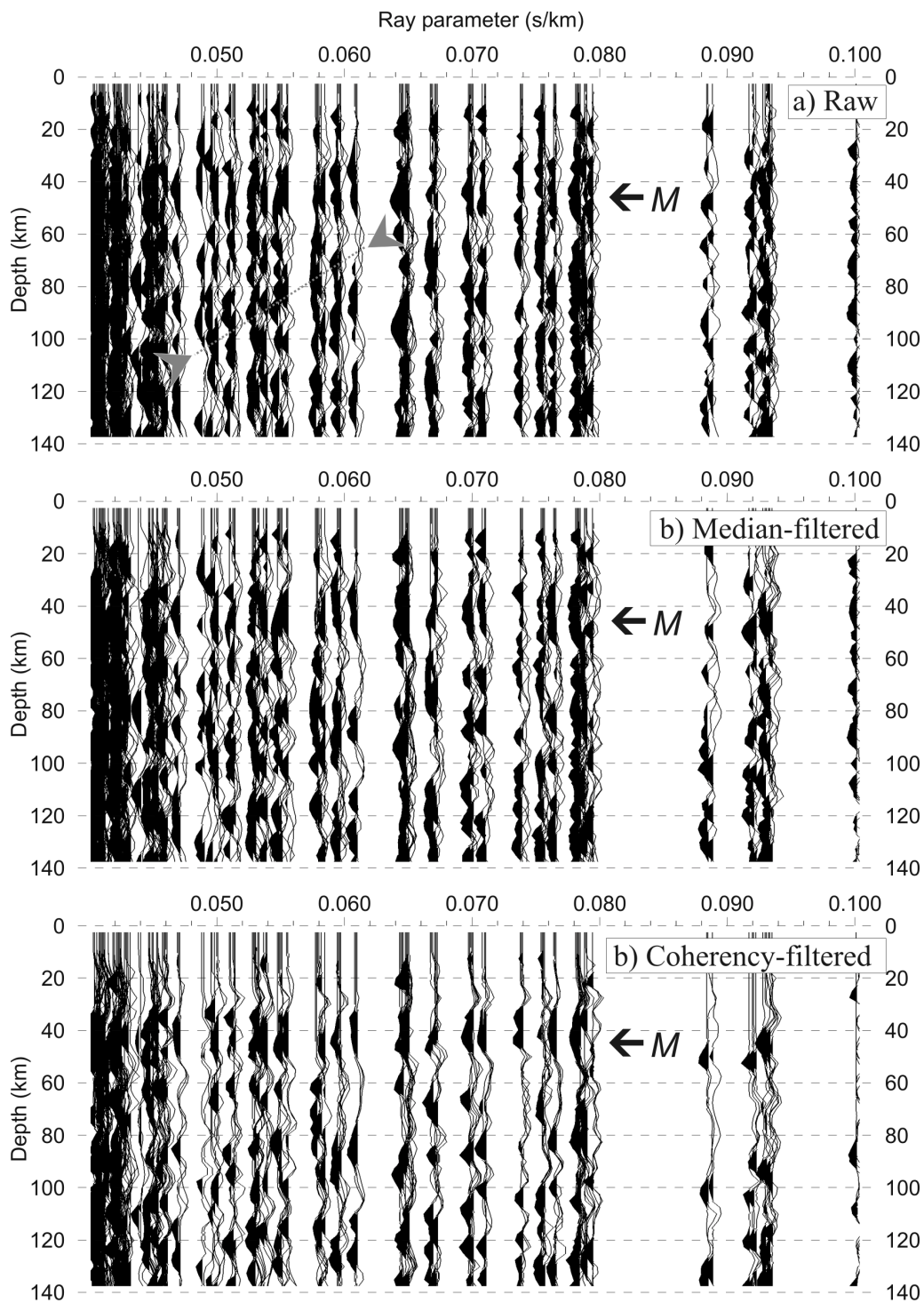
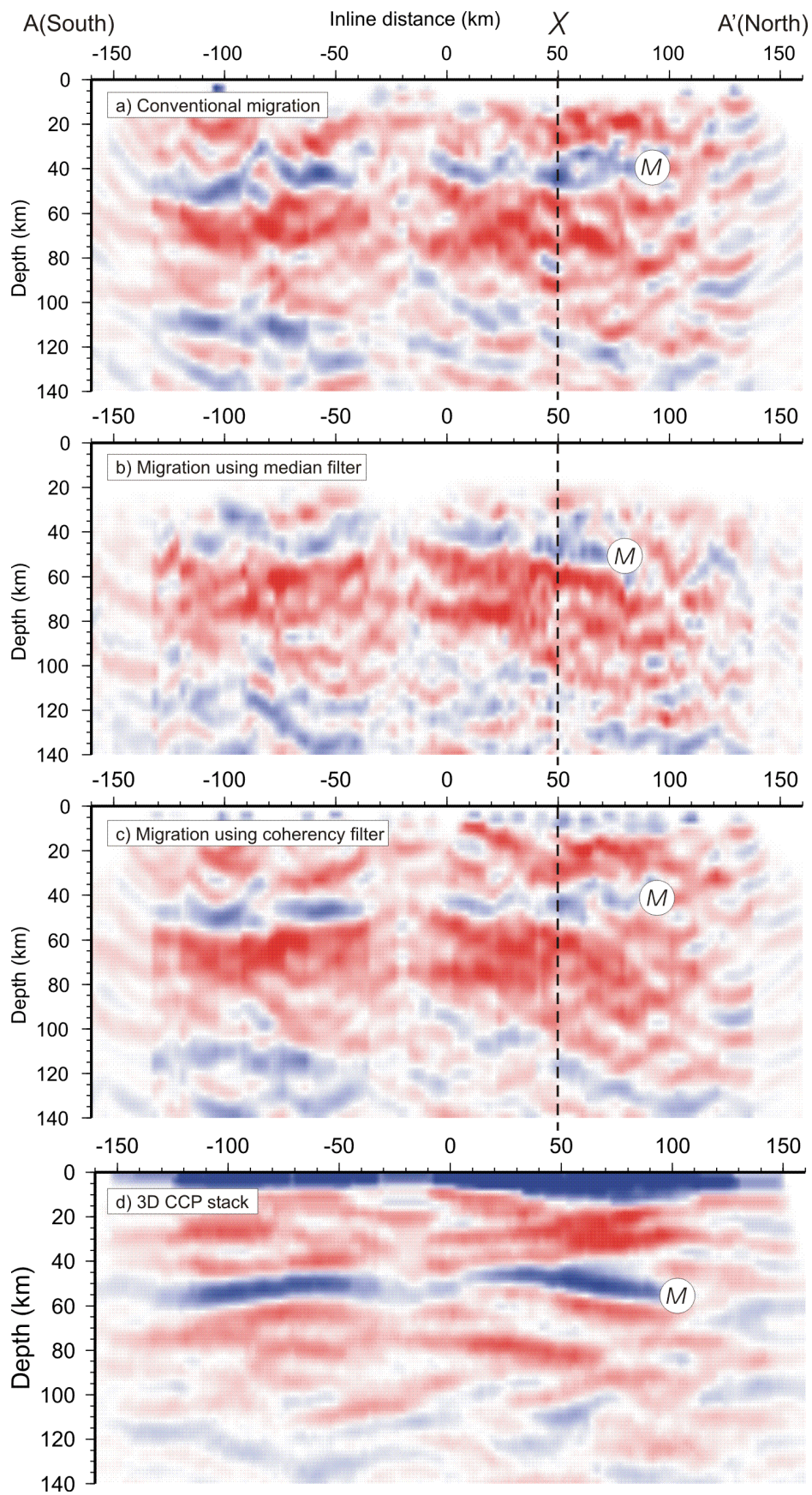


Fig. 4. A slice of the migrated 3-D image along the axis of the imaging grid (gray line in Fig. 2), using three different signal detection techniques illustrated in Fig. 3: (A) using the diffraction-stack pre-stack depth migration (Fig. 3a); (B) using the same kinematics and amplitude weighing as in the migration, but applying a median filter at every depth point (Fig. 3b); (C) using DDP migration with a built-in coherency filter rejecting the non-zero *depth vs. ray parameter* moveouts in the CIGs (Fig. 3d). Blue corresponds to positive and red to negative amplitudes, respectively. Note the differences in the images below the Moho (labeled M) and the different degrees of migration noise (“smiles”) near the edges of the images. (D) Axial slice of 3-D CCP stack (Fig. 2) obtained using the DDP method (Fig. 6; see discussion in the text). Due to conditioning by the 20-km bin sharing the Moho image is significantly more coherent than in the migrated images and most of the sub-Moho features appear sub-horizontal.



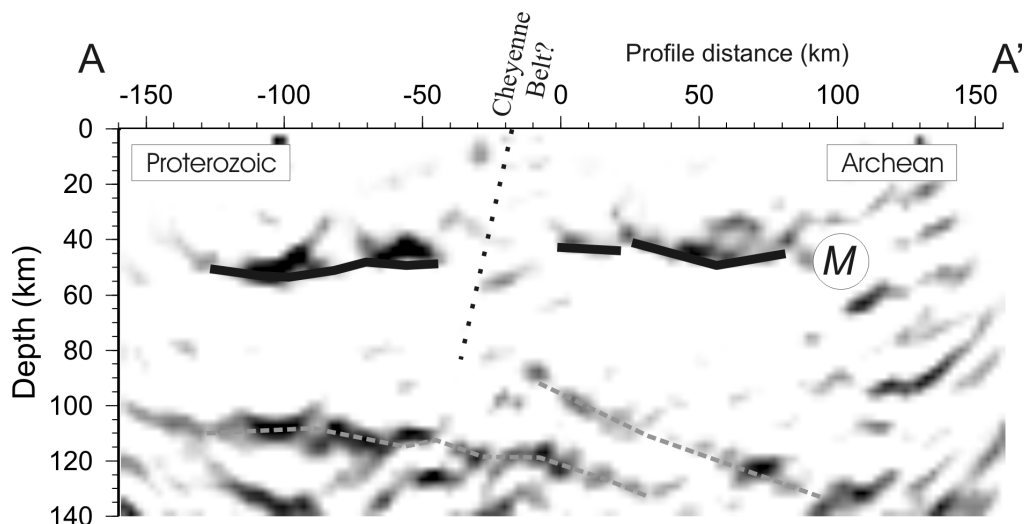


Fig. 5. Interpretation of the common features of the images in Fig. 4 (the image is from Fig. 4c).

The different migration techniques consistently indicate the Moho (labeled M) with a gap near Cheyenne Belt, and a thicker Proterozoic crust south of it, and north-dipping structures at 90-120 km depth (highlighted with gray dashed lines (make lines bigger maybe?)). The projection of the Cheyenne belt suture could be inferred from the gap in the Moho and truncation of the upper of the two mantle features, to 80-100 km depth. Gray shading shows only positive amplitudes.

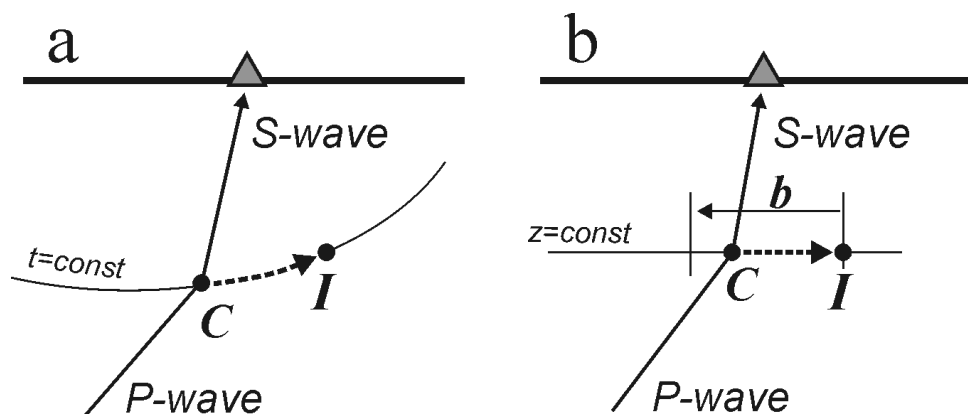


Fig. 6. Comparison of the time-to depth mapping used in pre-stack depth migration (a) and CCP stacking (b). In migration, the RF amplitude at conversion point C is mapped into the imaging points I located on a scattering ellipse corresponding to a constant $P_D S$ conversion time. In CCP stacking, a “piercing” point C is determined using station and source coordinates and assuming a horizontally layered structure. This point is migrated horizontally into the imaging points I located within a bin sharing distance b from C .

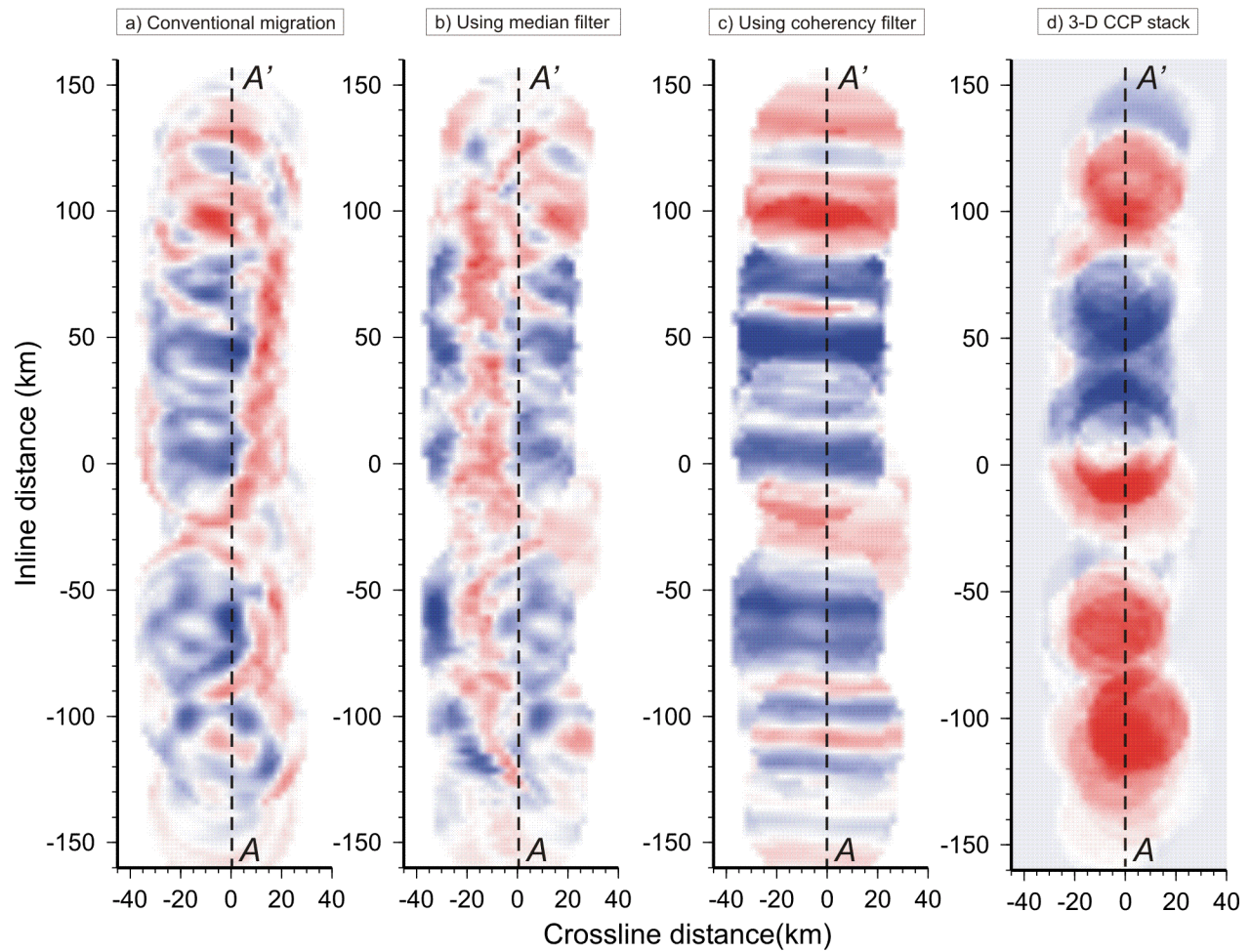


Fig. 7. Horizontal slice at 45-km depth through the migrated images in Fig. 4. Note the differences in the patterns of migrated and CCP images.